Antiferromagnetic character of the quantum phase transition in the Hubbard model on the honeycomb lattice

Johann Ostmeyer [ORCID],[1] Evan Berkowitz [ORCID],[2,3] Stefan Krieg [ORCID],[3,4,1] Timo A. Lähde [ORCID],[3,5] Thomas Luu [ORCID],[3,5,1] and Carsten Urbach [ORCID][1]

[1]*Helmholtz-Institut für Strahlen- und Kernphysik, Rheinische Friedrich-Wilhelms-Universität Bonn, 53115 Bonn, Germany*
[2]*Maryland Center for Fundamental Physics, University of Maryland, College Park 20742, USA*
[3]*Institute for Advanced Simulation, Forschungszentrum Jülich, 54245 Jülich, Germany*
[4]*JARA and Jülich Supercomputing Center, Forschungszentrum Jülich, 54245 Jülich, Germany*
[5]*Institut für Kernphysik, Forschungszentrum Jülich, 54245 Jülich, Germany*

We provide a unified, comprehensive treatment of all operators that contribute to the antiferromagnetic, ferromagnetic, and charge-density-wave structure factors and order parameters of the hexagonal Hubbard Model. We use the Hybrid Monte Carlo algorithm to perform a systematic, carefully controlled analysis in the temporal Trotter error and of the thermodynamic limit. We expect our findings to improve the consistency of Monte Carlo determinations of critical exponents. We perform a data collapse analysis and determine the critical exponent $\beta = 0.898(37)$ for the semimetal-Mott insulator transition in the hexagonal Hubbard Model. Our methods are applicable to a wide range of lattice theories of strongly correlated electrons.

I. INTRODUCTION

The Fermi-Hubbard model—a prototypical model of electrons hopping between lattice sites [1]—has a rich phenomenology of strongly correlated electrons requiring nonperturbative treatment [2]. On a honeycomb lattice, where it provides a basis for studying electronic properties of carbon nanosystems like graphene and nanotubes, the Hubbard model is expected to exhibit a second-order quantum phase transition between a (weakly coupled) semimetallic (SM) state and an antiferromagnetic Mott insulating (AFMI) state as a function of the electron-electron coupling [3].

It is noteworthy that a fully controlled *ab initio* characterization of the SM-AFMI transition has not yet appeared; Monte Carlo (MC) calculations have not provided unique, generally accepted values for the critical exponents [4,5]. Such discrepancies are primarily attributed to the adverse scaling of MC algorithms with spatial system size L and inverse temperature β. The resulting systematic error is magnified by an incomplete understanding of the extrapolation of operator expectation values to the thermodynamic and temporal continuum limits.

Lattice Monte Carlo (LMC) simulation of Hamiltonian and Lagrangian theories of interacting fermions is a mature field of study, which is seeing tremendous progress in the areas of novel computer hardware, algorithms, and theoretical developments. Efficient Hybrid Monte Carlo (HMC) algorithms [6,7] designed for theories with dynamical fermions, coupled with GPU-accelerated supercomputing [8], now allow for the direct simulation of systems of the same size as those used in realistic condensed-matter experiments and applications [9].

While much of the focus of LMC efforts continues to be on Lattice QCD, the algorithms and methods so developed

are now rapidly finding their place among the large variety of Hamiltonian theories in condensed matter physics. Recently, preliminary studies of nanotubes [10,11] have appeared and treatments of the Fermion sign problem based on formal developments [12,13] have made promising progress toward first-principles treatments of fullerenes [14] and doped systems [15]. Moreover, our understanding of these algorithms' ergodicity properties [16] and computational scaling [17,18] has also recently been placed on a firm footing.

In this work we seek to remove, using LMC techniques, the systematic uncertainties that affect determinations of the critical exponents of the SM-AFMI transition in the honeycomb Hubbard model. We present a unified, comprehensive, and systematically controlled treatment of the anti-ferromagnetic (AFM), ferromagnetic (FM), and charge-density-wave (CDW) order parameters and confirm the AFM nature of the transition from first principles. Building on our determination of the Mott gap [5], we find that the critical coupling $U_c/\kappa = 3.835(14)$ and the critical exponents—expected to be the exponents of the SU(2) Gross-Neveu, or chiral Heisenberg, universality class [19,20]—to be $\nu = 1.181(43)$ and $\beta = 0.898(37)$.

II. METHOD

We formulate the grand canonical Hubbard model at half filling in the particle-hole basis and without a bare staggered mass. Its Hamiltonian reads

$$H = -\kappa \sum_{\langle x,y \rangle} (p_x^\dagger p_y + h_x^\dagger h_y) + \frac{U}{2} \sum_x \rho_x \rho_x, \qquad (1)$$

where p and h are fermionic particle and hole annihilation operators, κ is the hopping amplitude, U the on-site interaction,

and

$$\rho_x = p_x^\dagger p_x - h_x^\dagger h_x \tag{2}$$

is the charge operator. Using Hasenbusch-accelerated [7,18] HMC [6] with the BRS formulation [21,22] and a mixed time differencing [5,10,22], which has favorable computational scaling and ergodicity properties [16], we generate ensembles of auxiliary field configurations for different linear spatial extents L with a maximum of $L = 102$ corresponding to 20,808 lattice sites, interaction strengths U (with fixed hopping κ), inverse temperatures $\beta = 1/T$, and N_t Trotter steps.[1] See Ref. [5] for full details.

We have used these ensembles to compute the Mott gap Δ as a function of U and β to locate a quantum critical point (QCP) at $T = 0$ [5] using finite-size scaling (FSS) [23–25]. The single-particle gap Δ was found to open at $U/\kappa = 3.834(14)$. Though this is widely expected to coincide with a semimetal-AFMI transition, we did not characterize the nature of the transition in Ref. [5]. Instead, we found the correlation length exponent $\nu = 1.185(43)$ from first principles and estimated the critical exponent $\beta_{\mathrm{mf}} = 1.095(37)$ for the staggered magnetization m_s under the AFMI assumption and the *mean-field* expectation $m_s \sim \Delta/U$ [26]. In this work we forgo these assumptions and confirm the AFMI character of the transition, finding $\beta = 0.898(37)$ in terms of a FSS analysis in the inverse temperature β.

Since the two values for β are strictly incompatible (5σ difference), our new results prove that the mean-field approximation is not well suited to extract critical exponents in the given model.

At half filling, we compute expectation values of one-point and two-point functions of bilinear local operators, the spins

$$S_x^i = \tfrac{1}{2}[p_x^\dagger, (-1)^x h_x]\sigma^i[p_x, (-1)^x h_x^\dagger]^\top \tag{3}$$

and the charge (2), where the σ^i are Pauli matrices and $(-1)^x$ provides a minus sign depending on the triangular sublattice of the honeycomb to which the site x belongs; the sign originates in the particle-hole transformation. For operators, we consider the uniform magnetization

$$S_+^i = \sum_x S_x^i, \tag{4}$$

where spins are summed coherently, and the staggered magnetization

$$S_-^i = \sum_x (-1)^x S_x^i, \tag{5}$$

which computes the difference between the sublattices. We expect the extensive one-point functions, the FM magnetization $\langle S_+^i \rangle$, AFM magnetization $\langle S_-^i \rangle$, the total charge $\langle \rho_+ \rangle$, and the charge separation $\langle \rho_- \rangle$ (and their respective intensive one-point functions) to vanish by symmetry at half filling for all β and U. However, the two-point functions,

$$S_{\pm\pm}^{ii} = \langle\langle S_\pm^i S_\pm^i \rangle\rangle, \tag{6}$$

and

$$Q_+^2 = \langle\langle \rho_+ \rho_+ \rangle\rangle, \quad Q_-^2 = \langle\langle \rho_- \rho_- \rangle\rangle, \tag{7}$$

need not vanish at half filling. The double-bracket notation indicates the connected correlator,

$$\langle\langle \mathcal{O}_1 \mathcal{O}_2 \rangle\rangle = \langle \mathcal{O}_1 \mathcal{O}_2 \rangle - \langle \mathcal{O}_1 \rangle \langle \mathcal{O}_2 \rangle. \tag{8}$$

These quantities scale quadratically with the spatial volume.[2] V which must be divided out to compute their respective intensive partners, which we denote with lowercase letters. For example, $s_{\pm\pm}^{ii} = S_{\pm\pm}^{ii}/V^2$ and similarly for q^2 and q_-^2. A *finite* nonvanishing s_{++}^{ii} (s_{--}^{ii}) indicates FM (AFM) order, while a nonvanishing q_-^2 indicates CDW order.[3]

On the other hand, at very low temperatures, any finite nonzero value of s_{++}^{ii}, s_{--}^{ii}, or q_-^2 corresponds to an extensive FM spin structure factor $S_F = S_{++}^{ii}/V$, AFM spin structure factor $S_{\mathrm{AF}} = S_{--}^{ii}/V$, or staggered charge structure factor $S_{\mathrm{CDW}} = Q_-^2/V$, respectively, diverging linearly with the spatial volume. The finite temperatures we use, however, provide a natural infrared cutoff for the correlation length, allowing different domains to cancel against one another. Because the dynamical exponent $z = 1$ [27] we can obtain intensive order parameters at any finite temperature by taking the thermodynamic limit of these extensive quantities and dividing them by β^2, rather than the spatial volume V. Finally, we use FSS in β to remove the infrared regulator and determine zero-temperature properties.

We decompose the observables of interest into a set of operators with zero, one, or two fermion bilinears, each on a definite sublattice, and evaluate each separately. This decomposition makes it easy to test the operators' individual behaviors in both noninteracting $U \to 0$ and nonhopping $\kappa \to 0$ limits, which are analytically known. We can also verify their expected scaling behaviors in Trotter error and volume. We reconstruct the operators of physical interest by taking the appropriate linear combination.

Constructing spin structure factors from fundamental operators

For a fully systematic treatment of the different spin operators, we express these in terms of 15 operators $O_{0...14}$ of one or two bilinear operators. Our basis of operators is complete for translationally invariant equal-time observables (the generalization is straightforward) and we can express the observables of physical interest as linear combinations of the operators in our basis.

Our basis fixes one position on a sublattice. We choose the operators with odd (even) index to act on $x \in A$ (B). As we do not break the sublattice symmetry explicitly, we can always consider these pairs of operators simultaneously. An overview

---

[1]Throughout this work, we use an upright β for the critical exponent and a slanted β for the inverse temperature.

[2]Here, V denotes the number of unit cells—half the number of lattice sites. Thus $V = L^2$ in case of an $L \times L$ lattice.

[3]Susceptibilities, like the AFM susceptibility χ_{AF}, can be reconstructed from these observables at half filling.

TABLE I. Extensive operators O_i. Spin comes with a factor 1/2; therefore the linear operators $O_{1,2}$ have to be divided by 2 and the quadratic ones $O_{3,\ldots,14}$ by 4. Sums over repeated indices are implicit and so is the addition of the term with $p \leftrightarrow h$. The two sites x and y are on the same lattice if $x \sim y$. We define $\mathrm{Ti}_x M := \mathrm{Tr}_S M^{-1}$ and $\mathrm{Rt}_x M := \mathrm{ReTr}_S M^{-1}$, where S is the sublattice containing x. Analogously, $\mathbb{P}_x$ is the projector onto the sublattice containing x. The error estimation comes from an exact calculation of $\mathrm{Rt}_x M$ at finite temperature and discretization in the noninteracting limit. The exact values in the two limits $U = 0$ and $\kappa = 0$ are given for zero temperature. We use the Bachmann-Landau notation to denote that an error in $\Theta(x)$ scales exactly as x, an error in $\mathcal{O}(x)$ scales maximally as x, and an error in $o(x)$ is asymptotically smaller than x.

O_i	Lattice	Operator/Implementation	$U = 0$	$\kappa = 0$	Error	Diagram
0		$\mathbb{1}$	V	V	0	
1,2		$p_x p_x^\dagger$ $\mathrm{Rt}_x M$	V	V	$\Theta(V\delta)$	
3,4	$x \sim y$	$p_x p_x^\dagger h_y h_y^\dagger$ $\frac{2}{V}\lvert \mathrm{Ti}_x M \rvert^2$	$V/2$	V	$\Theta(V\delta^2)$	
5,6	$x \nsim y$	$p_x p_x^\dagger h_y h_y^\dagger$ $\frac{2}{V}\mathrm{Re}\,\mathrm{Ti}_x M\,\mathrm{Ti}_y M^\dagger$	$V/2$	0	$\mathcal{O}(V\delta^2)$	
7,8	$x \sim y$	$p_x^\dagger h_x^\dagger h_y p_y$ $1 - \frac{2}{V}(\mathrm{Rt}_x M + \mathrm{Ti}_x M \mathbb{P}_y M^\dagger)$	$1/2$	V	$\Theta(\delta)$	
9,10	$x \nsim y$	$p_x^\dagger h_x^\dagger h_y p_y$ $\frac{1}{V}(\mathrm{Ti}_x M \mathbb{P}_y M^\dagger + \mathrm{Ti}_y M \mathbb{P}_x M^\dagger)$	$1/2$	V	$\mathcal{O}(\delta)$	
11,12	$x \sim y$	$p_x p_x^\dagger p_y p_y^\dagger$ $\frac{2}{V}(\mathrm{Rt}_x M + \mathrm{Re}(\mathrm{Ti}_x M)^2 - \mathrm{Ti}_x M \mathbb{P}_x M)$	$(V+1)/2$	V	$\Theta(V\delta^2)$	
13,14	$x \nsim y$	$p_x p_x^\dagger p_y p_y^\dagger$ $\frac{2}{V}(\mathrm{Re}\,\mathrm{Ti}_x M\,\mathrm{Ti}_y M - \mathrm{Re}\,\mathrm{Ti}_y M \mathbb{P}_x M)$	$(V-1)/2$	0	$\mathcal{O}(V\delta^2)$	

of the O_i based on the fermion matrix from [5]

$$M^{AA}_{(x,t)(y,t')} = \delta_{xy}(\delta_{t+1,t'} - \delta_{t,t'}\exp(-i\tilde\phi_{x,t})),$$
$$M^{BB}_{(x,t)(y,t')} = \delta_{xy}(\delta_{t,t'} - \delta_{t-1,t'}\exp(-i\tilde\phi_{x,t})), \qquad (9)$$
$$M^{AB}_{(x,t)(y,t')} = M^{BA}_{(x,t)(y,t')} = -\tilde\kappa\,\delta_{\langle x,y\rangle}\delta_{t,t'},$$

is given in Table I, and the various order parameters and structure factors are given in terms of the O_i in Table II, along with the exact values of the physical observables in the $\kappa = 0$ and $U = 0$ limits and their leading error terms. It should be noted that maximal ordering is not reached for $\beta < \infty$; thus the

observables for $\kappa = 0$ are limited by the temporal correlation length (the largest inverse Matsubara frequency β/π).

Let us consider the limits of no interaction ($U = 0$) and no hopping ($\kappa = 0$), for which the various observables can be exactly calculated for $T = 0$ ($\beta \to \infty$). We start with the particle/hole number ($i = 1, 2$ in Table I) which simply equals the number of unit cells V at half filling. Next, we consider the correlator between a particle and a hole ($i = 3 - 6$ in Table I). For $U = 0$, a particle does not see the holes. Therefore it is equally likely to encounter a hole on the same sublattice as a given particle as it is to find a hole on the other sublattice. As there are V holes in total, we find $V/2$ for each sublattice

TABLE II. Summary of physical observables (linear magnetizations and structure factors). The prime indicates that a given value can vary significantly due to finite temperature. In particular, $0'$ only goes to zero at $\beta \to \infty$ and $V' \approx \min(V, (\kappa\beta/\pi)^2)$. We use the Bachmann-Landau notation to denote that an error in $\Theta(x)$ scales exactly as x, an error in $\mathcal{O}(x)$ scales maximally as x, and an error in $o(x)$ is asymptotically smaller than x.

Observable	Definition	$U = 0$	$\kappa = 0$	Error
$\langle s_-^3\rangle$	$\frac{1}{2}\langle O_1 - O_2\rangle /V$	0	0	$o(\delta)$
$\langle s_+^3\rangle$	$1 - \frac{1}{2}\langle O_1 + O_2\rangle /V$	0	0	$\Theta(\delta)$
S_{--}^{11}/V	$\frac{1}{4}\langle O_7 + O_8 + O_9 + O_{10}\rangle$	$1/2$	V'	$\Theta(\delta)$
S_{--}^{33}/V	$\frac{1}{4}\langle O_3 + O_4 - O_5 - O_6 + O_{11} + O_{12} - O_{13} - O_{14}\rangle$	$1/2$	V'	$o(V\delta^2)$
S_{++}^{11}/V	$\frac{1}{4}\langle O_7 + O_8 - O_9 - O_{10}\rangle$	$0'$	$0'$	$\mathcal{O}(\delta)$
$\langle S_+^3 S_+^3\rangle /V$	$V - \langle O_1 + O_2\rangle + \frac{1}{4}\sum_{i\in\{3\ldots6,11\ldots14\}}\langle O_i\rangle$	$0'$	$0'$	$\Theta(V\delta^2)$
S_{++}^{33}/V	$\langle S_+^3 S_+^3\rangle - V\langle s_+^3\rangle^2$	$0'$	$0'$	$o(V\delta^2)$
Q_-^2/V	$\frac{1}{4}\langle -O_3 - O_4 + O_5 + O_6 + O_{11} + O_{12} - O_{13} - O_{14}\rangle$	$1/2$	$0'$	$o(V\delta^2)$

combination. For $\kappa = 0$, the lattice is frozen in a state of single up- or down-electrons per site with alternating sign. In terms of particles and holes, this translates to every A site having a particle and a hole and every B site having neither (or vice versa). Thus, a particle on a given site is perfectly correlated with all the holes on the same sublattice.

The coexistence of a particle and a hole as a pair in an excitonlike state ($i = 7 - 10$ in Table I) can be understood by a very similar consideration. At $U = 0$ a particle is (due to charge conservation) only responsible for the existence of a single hole which can be on the same or the other sublattice yielding a correlator of $1/2$; $\kappa = 0$, on the other hand, leads to a maximal correlation between particles and holes as they can only coexist in pairs.

It remains to consider correlations between particles ($i = 11 - 14$ in Table I) which behave completely similarly to the particle-hole correlation but for the difference of self-correlation. This is not relevant in the case without hopping because it is maximally correlated anyway. In the noninteracting case, however, there are on average $(V + 1)/2$ particles on the sublattice that contains the given particle and $(V - 1)/2$ particles on the other sublattice.

III. MEASUREMENTS AND EXTRAPOLATION

By inverting the fermion matrix on stochastic Fourier sources (see Appendix), we can compute fermion propagators and use Wick's theorem to contract the propagators into the relevant observables of interest (see Table I). Our structure factors measure two-point correlations between two bilinear operators at equal time; to fully exploit each configuration, we leverage time-translation invariance and average measurements on many time slices. Finally, the average of all measurements across the configurations within an ensemble with fixed U, β, Trotter discretization N_t, and spatial extent L gives an estimator for each observable.

We find that for both the AFM and the FM spin operators, the $i = 1$ and 3 components for $\langle\langle S^i S^i \rangle\rangle$ give different results configuration by configuration and ensemble averaged.[4] This is expected since our discretization breaks chiral symmetry which would have otherwise ensured their equality [28]. However, the mixed differencing of our discretization mitigates this breaking compared with a purely forward or purely backward differencing. Furthermore, in the continuum limit this symmetry is restored. Indeed, we observe that after continuum limit extrapolation, the different components agree up to uncertainties. We therefore directly take

$$m_s^2 = \frac{\sum_i S_{--}^{ii}}{V(\kappa\beta)^2} = \frac{2S_{--}^{11} + S_{--}^{33}}{V(\kappa\beta)^2} \tag{10}$$

as the staggered magnetization (and AFMI order parameter), simplifying the subsequent analysis.

For each U and β, we perform a simultaneous continuum- and infinite-spatial-volume extrapolation. For numerical tractability, we extrapolate extensive quantities, for example S_{AF}, which is kept finite by the IR regulation provided by the finite temperature.

_____

[4]Note that $S_{--}^{11} = S_{--}^{22}$ at the operator level.

A. Extrapolation formulas

The formulas used for the simultaneous thermodynamic and continuum limit extrapolation differ depending on the particular observable. There are, however, several rules applying to all of them. First, the leading-order error in the time discretization is exactly linear $\Theta(\delta)$, though the coefficient is significantly reduced by our mixed differencing scheme. Next, in Ref. [5], we showed that the spatial leading-order error has to be $\Theta(L^{-3})$ with the exception of observables prone to ensemblewise positive (or negative) definite deviations. These observables cannot average out local errors over the MC history and end up with an error in $\Theta(L^{-2})$. Unfortunately, the quadratic observables S_{--}^{ii} and m_s [Eqs. (12) and (13)] fall into this category.

From this starting point we derived the fit functions for all the magnetic observables by minor modifications. These modifications had to be made either because the leading-order terms did not describe the data well enough [Eq. (14)] or because the in principle leading coefficient in δ [Eq. (15)] or L [Eqs. (16) and (17)] could not be resolved numerically. A summary of the extrapolation formulas looks as follows:

$$\langle s_+^3 \rangle = s_{+,0}^3 + c_0^{s_+^3} \delta + c_1^{s_+^3} \delta L^{-3} \tag{11}$$

$$S_{AF} = S_{AF,0} + c_0^{S_{AF}} \delta + c_1^{S_{AF}} L^{-2} \tag{12}$$

$$\kappa\beta m_s = \kappa\beta m_{s,0} + c_0^{m_s} \delta + c_1^{m_s} L^{-2} \tag{13}$$

$$S_F^{11} = S_{F,0}^{11} + c_0^{S_F^{11}} \delta + c_1^{S_F^{11}} \delta^2 + c_2^{S_F^{11}} L^{-3} + c_3^{S_F^{11}} \delta L^{-3} \tag{14}$$

$$\langle S_+^3 S_+^3 \rangle / V = S_{F,0}^{33} + c_0^{S_F^{33}} \delta^2 L^2 \tag{15}$$

$$S_F^{33} = S_{F,0}^{33} + c_1^{S_F^{33}} \delta \tag{16}$$

$$S_{CDW} = S_{CDW,0} + c_0^{S_{CDW}} \delta. \tag{17}$$

There are two notable exceptions from the approach explained above. First, equation (11) for $\langle s_+^3 \rangle$ can be derived analytically in the noninteracting limit. It turns out that the equation captures the leading-order contributions very well even at finite coupling; $\langle s_-^3 \rangle$, on the other hand, is always compatible with zero, even at finite δ and L, and is therefore not extrapolated at all.

We provide two examples for the simultaneous extrapolations in Fig. 1. In the left panel we demonstrate the agreement of the data for the order-parameter m_s with the employed fit function (13) even in the case of very small statistical errors. Let us, with a look at the right panel, stress the importance of considering when to use the simple average $\langle \mathcal{O}_1 \mathcal{O}_2 \rangle$ and when to use the connected version $\langle\langle \mathcal{O}_1 \mathcal{O}_2 \rangle\rangle$. In the plot we clearly see the divergence of $\langle S_+^3 S_+^3 \rangle$ in spatial volume as predicted in Eq. (15). This divergence foils any attempt of a statistically significant extrapolation, though the continuum limit would in principle yield the correct result. Should a thermodynamic limit extrapolation be attempted before the continuum limit extrapolation, one would even end up with infinite values. It is, therefore, of crucial importance in this case to use $S_{++}^{33} = \langle\langle S_+^3 S_+^3 \rangle\rangle$ which is well behaved. On the other hand, it makes sense to use $\langle \mathcal{O}_1 \mathcal{O}_2 \rangle$ whenever $\langle \mathcal{O}_1 \rangle \langle \mathcal{O}_2 \rangle$ is known analytically to minimize noise. In
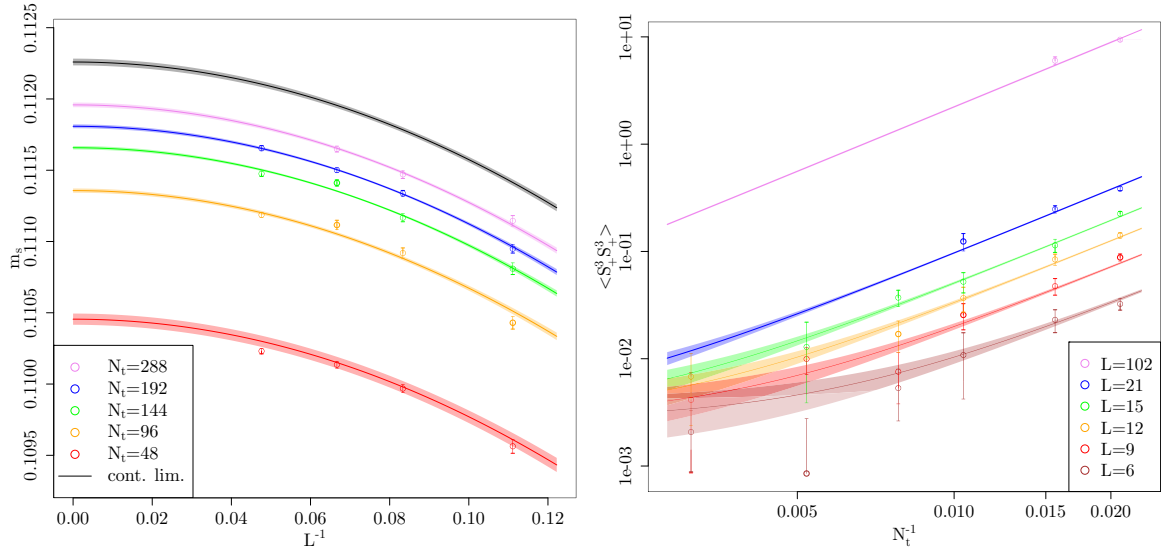
FIG. 1. Simultaneous two-dimensional fit of m_s using the extrapolation formula (13) for $\beta = 12$ and $U = 1$ (left) and $\langle S_+^3 S_+^3 \rangle$ using the extrapolation formula (15) for $\beta = 8$ and $U = 3.5$ (right). All quantities are in units of κ. The fits are performed for $L \geqslant 9$ and $N_t/\beta \geqslant 6$. The fit on the left (right) has $\chi^2/\text{d.o.f.} \simeq 1.6$ ($\chi^2/\text{d.o.f.} \simeq 1.1$), corresponding to a p-value of $\simeq 0.08$ ($\simeq 0.38$). Note the double-logarithmic scale in the right panel.

particular, $\langle S_-^i \rangle$ and $\langle S_+^1 \rangle$ both vanish, which is why the subtraction need only be performed for S_{++}^{33}.

B. Data collapse

As in Ref. [5], we use FSS relations to perform a simultaneous data collapse of m_s and the gap Δ and thus remove the dependence on β in each of these quantities. The collapse for m_s is depicted in the left panel of Fig. 2. Note that the data points below the transition, i.e., $U - U_c < 0$, collapse to a single curve, whereas above the transition the points for different β start to deviate because of the infrared cutoff imposed by our finite β calculations. This effect has regularly been observed before; see, for example, Fig. 7 in Ref. [2] and Fig. 3 in Ref. [29]. For larger β the collapse of the curve persists for a wider range above the transition. Points with an obvious

deviation from the global curve have been excluded from the fit so that a bias is avoided. Since the collapse fit in Δ, as done independently in Ref. [5] yielding $U_c/\kappa = 3.834(14)$ and $\nu = 1.185(43)$, requires only two free parameters U_c and ν, it is more stable and statistically more significant than the collapse fit of m_s with the three free parameters U_c, ν, and β. We therefore performed the simultaneous collapse fit of both Δ and m_s giving the Δ fit a higher weight. We find

$$
\begin{aligned}
\beta &= 0.898(37), \\
\nu &= 1.181(43), \\
\beta/\nu &= 0.761(5), \\
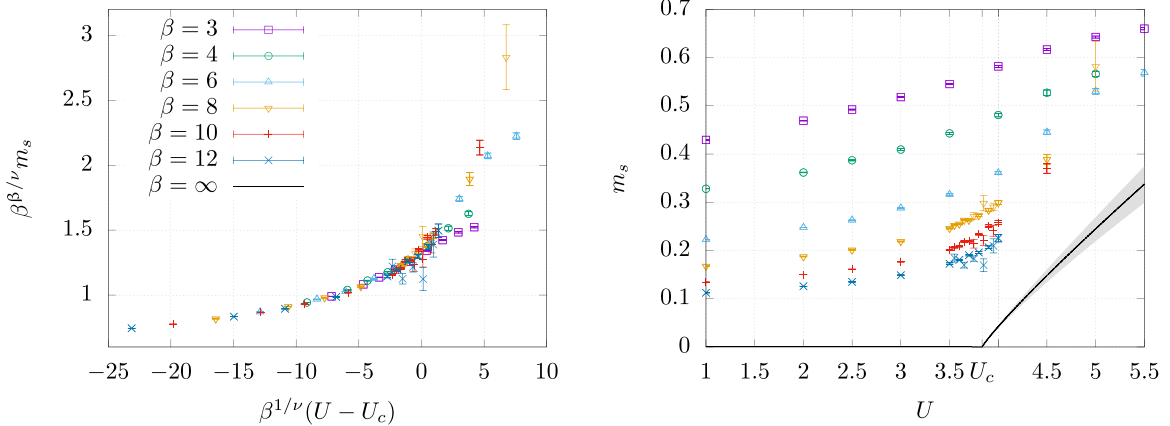U_c/\kappa &= 3.835(14).
\end{aligned} \tag{18}
$$

FIG. 2. Left: Data collapse plot with the optimal parameters of U_c, ν, and β obtained from a simultaneous collapse fit to the gap Δ and the order-parameter m_s. Note that the "outliers" are due to particularly small β and are excluded from the analysis. For $U < U_c \simeq 3.835(14)$, the order parameter vanishes. Right: The AFMI order-parameter (staggered magnetization) m_s, with all quantities in units of κ, after the thermodynamic and continuum limit extrapolations. We also show $m_s(U, \beta = \infty)$ as a solid black line with error band (calculated as in Ref. [5]). The legend from the left plot applies to both.
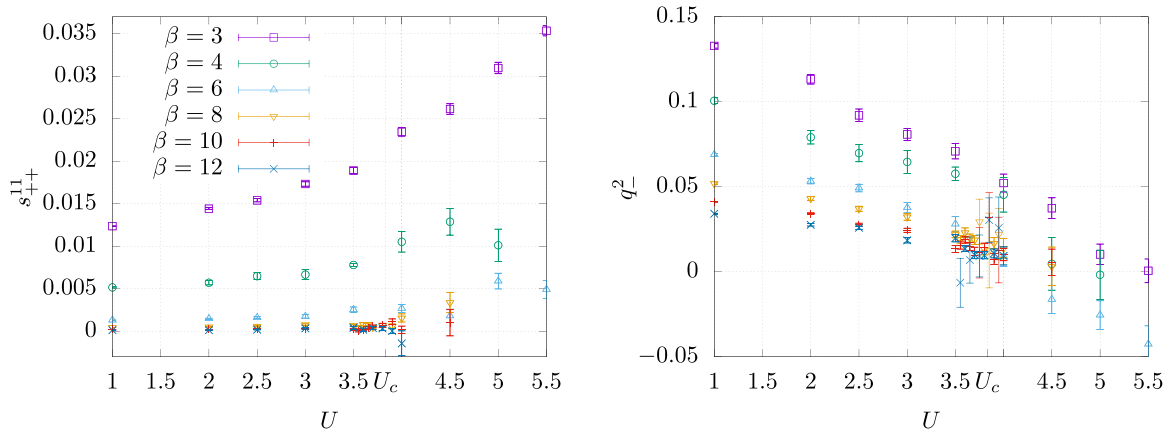
FIG. 3. FM (left) and CDW (right) order parameters at different couplings, with all quantities in units of κ, after the thermodynamic and continuum limit extrapolations. The legend from the left plot applies to both.

The critical coupling is essentially unchanged from our previous result [5].

The correlation matrix,

$$\text{corr}(U_c,\ \nu,\ \beta) = \begin{pmatrix} 1.0000 & -0.0395 & -0.1197 \\ -0.0395 & 1.0000 & 0.9944 \\ -0.1197 & 0.9944 & 1.0000 \end{pmatrix}, \tag{19}$$

clearly shows a strong correlation between ν and β, whereas U_c is weakly correlated. Put differently, the ratio $\beta/\nu = 0.761(5)$ can be determined with extremely high precision. We give enough digits to yield percent-level matching to our full numerical results when inverting the correlation matrix. We have also considered the inclusion of subleading corrections to the FSS analysis along the lines of Ref. [4], where an additional factor $1 + c_L L^{-\omega}$ was introduced into the scaling relation for m_s. While the FSS analysis in L of Ref. [4] found a clear signal for $c_L \neq 0$, an FSS analysis of our MC data with an additional factor $1 + c_\beta \beta^{-\omega'}$ turned out consistent with $c_\beta = 0$. For any choice of ω', we found that assuming $c_\beta \neq 0$ worsened the uncertainties of the extracted parameters, though these remained consistent with the values quoted for $c_\beta = 0$. We thus conclude that our MC data does not support the scenario of sizable subleading corrections to the scaling in β, at least within the statistical accuracy and range of temperatures covered by our present set of ensembles. As the (expected) Lorentz-invariance should only emerge in the vicinity of the QCP, this apparent difference in the subleading corrections may reflect the underlying structure of the Hubbard Hamiltonian.

The zero-temperature AFMI order-parameter $m_s(\beta = \infty)$ is also given in the right panel of Fig. 2. This has been determined from MC data extrapolated to infinite volume and the continuum limit using the same strategy as for the zero-temperature single-particle gap in Ref. [5]. We have extrapolated the $U/\kappa = 4$ values to $\beta = \infty$ and used that result to constrain the overall scale of m_s (given the critical exponents we have already fixed from FSS). Note that $m_s(\beta = \infty)$ so determined is expected to be strictly valid only in the vicinity of the QCP.

In Fig. 3, we show our continuum and thermodynamic limit extrapolations of the FM (s_{++}^{ii}) and CDW (q_-^2) order parameters. While q_-^2 is a strictly semipositive observable, we find that several individual values of q_i^2 are slightly negative (though with large error bars), in particular for large U/κ. This effect appears to be a consequence of residual extrapolation uncertainties, as our extrapolation does not enforce semipositivity. Still, we observe that both s_{++}^{ii} and q_-^2 clearly vanish in the zero-temperature ($\beta \to \infty$) limit for all U/κ. This behavior is in contrast to that of m_s, which remains nonzero for large U/κ, and confirms the AFM character of the QCP.

IV. DISCUSSION

We have presented the first fully systematic, high-precision treatment of all operators that contribute to the AFM, FM, and CDW order parameters of the Hubbard Model on a honeycomb lattice, followed by an FSS analysis of the SM-AFMI transition in the inverse temperature β, culminating in our results (18). Within the accuracy of our MC data, we find that the QCP associated with the SM-AFMI transition coincides with the opening of the single-particle gap Δ, which disfavors the possibility of other exotic phenomena (such as an intermediate spin-liquid phase [30,31]) in the vicinity of the critical coupling where the AFMI order-parameter m_s appears. Also, the vanishing of the FM and CDW order parameters throughout this transition strengthens the notion that the QCP is purely AFM in character.

In addition to an unambiguous classification of the character of the QCP of the honeycomb Hubbard model, our results demonstrate the ability to perform high-precision calculations of strongly correlated electronic systems using lattice stochastic methods. A central component of our calculations is the Hasenbusch-accelerated HMC algorithm, as well as other state-of-the-art techniques originally developed for lattice QCD. This has allowed us to push our calculations to system sizes which are, to date, still the largest that have been performed, up to 102×102 unit cells (or 20,808 lattice sites).

Our progress sets the stage for future high-precision calculations of additional observables of the Hubbard model and its extensions, as well as other Hamiltonian theories of strongly correlated electrons [32–34]. We anticipate the continued advancement of calculations with ever-increasing

system sizes through the leveraging of additional state-of-the-art techniques from lattice QCD, such as multigrid solvers on GPU-accelerated architectures. We are actively pursuing research along these lines.

APPENDIX: STOCHASTIC FOURIER SOURCES

We can estimate the trace of any matrix D with dimension d over a subset I_0 of the indices I using the established method of noisy estimators [39,40] as follows. Sample a vector χ randomly with all the elements χ_i independent and identically distributed[5] (iid), such that

$$\langle \chi \rangle = 0, \tag{A1}$$

$$\langle \chi_i^* \chi_j \rangle = \delta_{ij} \quad \text{if } i, j \in I_0, \tag{A2}$$

$$\chi_i = 0 \quad \text{if } i \in I \setminus I_0. \tag{A3}$$

Then the expectation value of $\chi^\dagger D \chi$, obtained by repeated calculation, yields the desired trace,

$$\text{Tr}_{I_0} D = \langle \chi^\dagger D \chi \rangle. \tag{A4}$$

1. Comparison of different sources

Reference [40] gives an overview over the advantages and drawbacks of various distributions that can be employed for noisy trace estimation and also provides rigorous upper limits on the number of sources required to obtain a precision ε with a probability of at least $1 - \delta$. This upper bound in principle prefers Gaussian noise, but it is extremely loose and therefore not useful in practice. This is why we will not go into detail about these bounds. It suffices to know that such a bound exists and that the error on the trace estimation is proven to converge with $1/\sqrt{n}$ (as one would expect for a stochastic calculation) where n is the number of noisy sources.

The approach presented in Ref. [39] gives a guideline of how to identify efficient distributions that is far more useful. We present it here in a slightly modified form, but the

---

[5]We will later see that this is a sufficient but not a necessary condition.

conclusions are identical. Let us for now define χ^r to be the r-th noisy vector and $\langle \cdot \rangle$ to denote the exact expectation value (where we usually use it for the MC average). Then the two quantities

$$C_1(i) := \left| \left\langle \frac{1}{n} \sum_r |\chi_i^r|^2 \right\rangle - 1 \right| \tag{A5}$$

$$\text{and} \quad C_2(i, j) := \sqrt{\frac{1}{n} \left\langle \left| \sum_r \chi_i^{r*} \chi_j^r \right|^2 \right\rangle}, \; i \neq j \tag{A6}$$

are good measures for the error. Here, $C_1(i)$ quantifies misestimation of the diagonal entries of the matrix and $C_2(i, j)$ gives the error due to the off-diagonal elements not being suppressed perfectly. Both $C_1(i)$ and $C_2(i, j)$ do not depend on the indices i, j as long as the χ_i are identically (not necessarily independently) distributed for every r. We therefore drop the dependencies from now on. The expectation value of the total error for a trace estimation then reads

$$\sigma = \frac{1}{\sqrt{n}} \sqrt{C_1^2 \sum_{i \in I_0} |D_{ii}|^2 + C_2^2 \sum_{i, j \in I_0, i \neq j} |D_{ij}|^2}. \tag{A7}$$

C_1 and C_2 are mostly independent from each other and we are going to minimize them individually in the following.

It is easy to see that C_1 can be eliminated completely by using noise on the complex unit circle, i.e., $|\chi_i^r| = 1$ for all i and r. This is besides others realized by (complex) Z2 noise which chooses with equal probability from $\{\pm 1\}$ ($\{\pm 1, \pm i\}$). Let us remark here that $C_1 = 0$ is a very important feature because noisy trace estimation is only efficient for diagonally dominated matrices. Z2 and similar noise calculate the trace of a diagonal matrix exactly with a single source, whereas other distributions, e.g., Gaussian noise, would still require a high number of sources to get a decent approximation.

On the other hand, C_2 is nearly independent of the distribution. In the cases where all χ_i^r are iid, one finds

$$\langle \eta^r \rangle = 0, \tag{A8}$$

$$\langle |\eta^r|^2 \rangle = \langle (\chi_i^{r*} \chi_j^r)^* \chi_i^{r*} \chi_j^r \rangle = \langle \chi_i^r \chi_i^{r*} \rangle \langle \chi_j^{r*} \chi_j^r \rangle = 1, \tag{A9}$$

where we defined $\eta^r := \chi_i^{r*} \chi_j^r$ and dropped the indices $i \neq j$ as before. Thus η^r is iid with zero expectation value and unit standard deviation. The central limit theorem now guarantees that for large r the distribution approaches $\sum_r \eta^r \sim \mathcal{N}_{0,n}$. Moreover, the variance is an additive quantity for independent variables which yields $C_2 = 1$ exactly.

This leads to the conclusion that any iid noise with numbers of unit modulus gives the same error and this error is the theoretically optimal one for iid noise.

In practice one is often not interested in the complete trace but, for example, in its real part only. Then real iid sources give the well-known result $C_2 = 1$. Remarkably, however, the same result also holds for complex noise where the deviation is split into the real and imaginary parts C_2^R and C_2^I, respectively, as $C_2^2 = C_2^{R2} + C_2^{I2}$. We observe that both projections can be minimized when $C_2^R = C_2^I = 1/\sqrt{2}$. This is the case in complex Z2 noise which is the reason why it is usually preferred over real Z2 noise.

Note that neither of the possible error contributions C_1 and C_2 contains the condition $\langle \chi \rangle = 0$ nor independence or identical distribution ($\langle \eta^r \rangle = 0$ in contrast is required). We are therefore going to drop these superfluous requirements and see if we can find an even more efficient method for trace estimations. As C_1 cannot be optimized any further, we only have to consider C_2, which is the average of all variances and covariances of η^r over r. We are now only considering noise with $|\chi_i^r| = 1$, so $|\eta^r| = 1$ as well and the variance of η^r is guaranteed to be 1 as before. Therefore the only variable one can optimize is the covariance of η^r,

$$\zeta^{rs} := \text{cov}(\eta^{r*}, \eta^s), \tag{A10}$$

with which we can rewrite the off-diagonal error contribution

$$
C_2 = \sqrt{\frac{1}{n}\left\langle \sum_{r,s} \eta^{r*}\eta^s \right\rangle} = \sqrt{\frac{1}{n}\left\langle \sum_r |\eta^r|^2 + \sum_{r\neq s} \eta^{r*}\eta^s \right\rangle}
$$

$$
= \sqrt{1 + \frac{1}{n}\sum_{r\neq s} \zeta^{rs}}. \tag{A11}
$$

The symmetry in r and s suggests that C_2 is minimized when all ζ^{rs} are equal and maximally negative. This optimum is, quite intuitively, reached for all χ^r pairwise orthogonal. In this case, the probability p_r of redundancy one would have for iid noise is reduced to $p_r - 1/(d-1)$ because one of the dimensions cannot be reached again. This difference already is the covariance we are looking for. Thus we obtain a lower bound for the error contribution

$$
C_2 \geqslant \sqrt{1 + \frac{1}{n}\sum_{r\neq s}\frac{-1}{d-1}} = \sqrt{1 - \frac{n(n-1)}{n(d-1)}} = \sqrt{1 - \frac{n-1}{d-1}}
$$

$$
= 1 - \frac{n}{2d} + \mathcal{O}(d^{-1}) + \mathcal{O}\left(\left(\frac{n}{d}\right)^2\right). \tag{A12}
$$

It is easy to convince oneself that this really is the optimum because the error vanishes for $n = d$ when one has sampled the full space. Therefore there is no deterministic nor stochastic algorithm that does not use any specific features of a given matrix and is more efficient than this method.

An efficient practical realization would be to draw

$$\chi_i^0 \sim \left\{ e^{i2\pi\frac{k}{d}} \,\middle|\, k \in \{0,\ldots,d-1\} \right\} \tag{A13}$$

iid and for all $r \geqslant 1$ to sample $j_r \in \{1,\ldots,d-1\}$ without repetition setting

$$\chi_i^r = e^{i2\pi\frac{i}{d}j_r}\chi_i^0. \tag{A14}$$

Last but not least, we emphasize that for the trace estimation to be useful one has to reach the desired accuracy at some $n \ll d$. So the tiny gain from choosing all noise vectors pairwise orthogonal is negligible in practice.

2. Second-order observables

The quartic operators $O_{3\ldots14}$ cannot be expressed in terms of simple traces. Instead we have to generalize the noisy source estimation. There are different possible approaches. In our simulations we chose to sample χ again as above, then define

$$\chi' = M^{-1}\chi, \tag{A15}$$

$$\chi'' = M^{\dagger^{-1}}\chi \tag{A16}$$

and estimate the relevant quantities as

$$\sum_{x,y\in A}|(M^{-1})_{(x,t),(y,t)}|^2 = \left\langle \sum_{x\in A}|\chi'_{x,t}|^2 \right\rangle, \tag{A17}$$

$$\sum_{x,y\in A}\left((M^{-1})_{(y,t),(x,t)}(M^{-1})_{(x,t),(y,t)}\right) = \left\langle \sum_{x\in A}\chi''^*_{x,t}\chi'_{x,t}\right\rangle. \tag{A18}$$

Note that the right-hand side term is not a simple scalar product $\chi'^\dagger \cdot \chi'$, respectively, $\chi''^\dagger \cdot \chi'$. We have to include the projection here explicitly. This allows to compute $\sum_{x\in A, y\in B}$ nearly without additional computational effort, as only the projection sum has to be adjusted, not the linear solve.

3. Average over time slices

For the structure factors the averages over the time slices have to be included explicitly and cannot be absorbed in the traces. This means that the number of linear solves increases from the number of noisy sources n to $N_t \cdot n$. As this is extremely expensive, we evaluate the average over all time slices by an average including only a fixed number of equidistant times, which is guaranteed to be equal in the infinite-statistics limit by translation invariance while saving computational cost without losing much accuracy, since neighboring time slices on any given configuration are correlated.

Another approach would be to sample χ not from, e.g., $I_0 = (A, t)$, but from I always and include the projection later,

$$\text{Tr}_{I_0}D = \sum_{i\in I_0, j\in I}\langle \chi_i^* D_{ij}\chi_j\rangle. \tag{A19}$$

Naïvely one would expect that this saves a lot of linear solves, but it also introduces a lot of additional noise. The variance of the sum in Eq. (A19) increases linearly in the cardinality of I. In order to compensate this increase in statistical fluctuations we would have to increase the number of noisy sources by the same amount. Thus at equal statistical precision the number of linear solves stays the same.

4. The time-shifted trace

In general, we have to not only calculate traces but also sums over off-diagonal matrix elements—correlators between operators at different times. This time shift can be implemented in the following way (again χ sampled as above):

$$\sum_t D_{t+\tau,t} = \sum_{t,t'}D_{t',t}\delta_{t',t+\tau} = \sum_{t,t'}D_{t',t}\langle \chi_{t'}^*\chi_{t+\tau}\rangle$$

$$= \left\langle \sum_t (D^\dagger\chi)_t^* \chi_{t+\tau}\right\rangle, \tag{A20}$$

where τ is an arbitrary time shift.

[1] J. Hubbard, Proc. R. Soc. London A **276**, 238 (1963).

[2] S. R. White, D. J. Scalapino, R. L. Sugar, E. Y. Loh, J. E. Gubernatis, and R. T. Scalettar, Phys. Rev. B **40**, 506 (1989).

[3] T. Paiva, R. T. Scalettar, W. Zheng, R. R. P. Singh, and J. Oitmaa, Phys. Rev. B **72**, 085123 (2005).

[4] Y. Otsuka, S. Yunoki, and S. Sorella, Phys. Rev. X **6**, 011029 (2016).

[5] J. Ostmeyer, E. Berkowitz, S. Krieg, T. A. Lähde, T. Luu, and C. Urbach, Phys. Rev. B **102**, 245105 (2020).

[6] S. Duane, A. D. Kennedy, B. J. Pendleton, and D. Roweth, Phys. Lett. B **195**, 216 (1987).

[7] M. Hasenbusch, Phys. Lett. B **519**, 177 (2001).

[8] M. A. Clark, R. Babich, K. Barros, R. C. Brower, and C. Rebbi, Comput. Phys. Commun. **181**, 1517 (2010).

[9] M. Ulybyshev, S. Zafeiropoulos, C. Winterowd, and F. Assaad, arXiv:2104.09655 [cond-mat.str-el] (2021).

[10] T. Luu and T. A. Lähde, Phys. Rev. B **93**, 155106 (2016).

[11] E. Berkowitz, C. Körber, S. Krieg, P. Labus, T. A. Lähde, and T. Luu, EPJ Web Conf. **175**, 03009 (2018).

[12] M. Cristoforetti, F. Di Renzo, and L. Scorzato (AuroraScience Collaboration), Phys. Rev. D **86**, 074506 (2012).

[13] T. Kanazawa and Y. Tanizaki, J. High Energy Phys. 03 (2015) 044.

[14] J.-L. Wynen, E. Berkowitz, S. Krieg, T. Luu, and J. Ostmeyer, Phys. Rev. B **103**, 125153 (2021).

[15] M. Ulybyshev, C. Winterowd, and S. Zafeiropoulos, Phys. Rev. D **101**, 014508 (2020).

[16] J.-L. Wynen, E. Berkowitz, C. Körber, T. A. Lähde, and T. Luu, Phys. Rev. B **100**, 075141 (2019).

[17] S. Beyl, F. Goth, and F. F. Assaad, Phys. Rev. B **97**, 085144 (2018).

[18] S. Krieg, T. Luu, J. Ostmeyer, P. Papaphilippou, and C. Urbach, Comput. Phys. Commun. **236**, 15 (2019).

[19] D. J. Gross and A. Neveu, Phys. Rev. D **10**, 3235 (1974).

[20] L. Janssen and I. F. Herbut, Phys. Rev. B **89**, 205403 (2014).

[21] R. Brower, C. Rebbi, and D. Schaich, arXiv:1101.5131v1 [hep-lat] (2011).

[22] R. Brower, C. Rebbi, and D. Schaich, Hybrid Monte Carlo simulation on the graphene hexagonal lattice, PoS **(Lattice 2011)**, 056 (2011).

[23] M. E. J. Newman and G. T. Barkema, *Monte Carlo Methods in Statistical Physics* (Clarendon Press, Oxford, 1999).

[24] A. Dutta, G. Aeppli, B. K. Chakrabarti, U. Divakaran, T. F. Rosenbaum, and D. Sen, Quantum Phase Transitions, in *Quantum Phase Transitions in Transverse Field Spin Models: From Statistical Physics to Quantum Information* (Cambridge University Press, Cambridge, 2015), pp. 3–31.

[25] H. Shao, W. Guo, and A. W. Sandvik, Science **352**, 213 (2016).

[26] F. F. Assaad and I. F. Herbut, Phys. Rev. X **3**, 031010 (2013).

[27] I. F. Herbut, Phys. Rev. Lett. **97**, 146401 (2006).

[28] P. Buividovich, D. Smith, M. Ulybyshev, and L. von Smekal, PoS **(LATTICE 2016)**, 244 (2016).

[29] P. Buividovich, D. Smith, M. Ulybyshev, and L. von Smekal, Phys. Rev. B **98**, 235129 (2018).

[30] Z. Y. Meng, T. C. Lang, S. Wessel, F. F. Assaad, and A. Muramatsu, Nature (London) **464**, 847 (2010).

[31] S. Sorella, Y. Otsuka, and S. Yunoki, Sci. Rep. **2**, 992 (2012).

[32] J. N. Leaw, H.-K. Tang, P. Sengupta, F. F. Assaad, I. F. Herbut, and S. Adam, Phys. Rev. B **100**, 125116 (2019).

[33] Y.-X. Zhang, W.-T. Chiu, N. C. Costa, G. G. Batrouni, and R. T. Scalettar, Phys. Rev. Lett. **122**, 077602 (2019).

[34] C. Chen, X. Y. Xu, Z. Y. Meng, and M. Hohenadler, Phys. Rev. Lett. **122**, 077601 (2019).

[35] Jülich Supercomputing Centre, J. Large-Scale Res. Facil. **4**, A132 (2018).

[36] N. Eicker, T. Lippert, T. Moschny, and E. Suarez, Concurr. Comput. **28**, 2394 (2016).

[37] R Core Team, *R: A Language and Environment for Statistical Computing*, R Foundation for Statistical Computing, Vienna, Austria (2018), https://www.R-project.org.

[38] B. Kostrzewa, J. Ostmeyer, M. Ueding, and C. Urbach, Hadron: Analysis Framework for Monte Carlo Simulation Data in Physics (2020), r package version 3.1.0, https://github.com/HISKP-LQCD/hadron.

[39] S.-J. Dong and K.-F. Liu, Phys. Lett. B **328**, 130 (1994).

[40] H. Avron and S. Toledo, J. ACM **58**, 1 (2011).